RESEARCH ARTICLE

A coupled SPFEM/DEM approach for multiscale modeling of large-deformation geomechanical problems

Ning Guo[1,2] | Zhongxuan Yang[1,2] | Weihai Yuan[3] | Jidong Zhao[4]

[1] Engineering Research Center of Urban Underground Space Development of Zhejiang Province, Zhejiang University, Hangzhou, Zhejiang 310058, China

[2] Computing Center for Geotechnical Engineering, Zhejiang University, Hangzhou, Zhejiang 310058, China

[3] College of Mechanics and Materials, Hohai University, Nanjing, Jiangsu 210098, China

[4] Department of Civil and Environmental Engineering, Hong Kong University of Science and Technology, Clearwater Bay, Kowloon, Hong Kong

Correspondence
Ning Guo, Engineering Research Center of Urban Underground Space Development of Zhejiang Province, Zhejiang University, Hangzhou, Zhejiang 310058, China.
Email: nguo@zju.edu.cn

Abstract

Computational modeling in geotechnical engineering frequently needs sophisticated constitutive models to describe prismatic behavior of geomaterials subjected to complex loading conditions, and meanwhile faces challenges to tackle large deformation in many geotechnical problems. The study presents a multiscale approach to address both challenges based on a hierarchical coupling of the smoothed particle finite element method (SPFEM) and the discrete element method (DEM) (coined SPFEM/DEM). In the approach, SPFEM serves as a solver for the global boundary value problem, in which the material constitutive responses are derived from the DEM solution of representative volume elements (RVEs) attached to the SPFEM nodes to avoid phenomenological constitutive assumptions. The approach is capable of modeling large deformation because of use of SPFEM, which discretizes the domain with a set of Lagrangian nodes and employs Delaunay triangulation for efficient remeshing on the nodes. In addition, as the RVEs are associated with the nodes due to the nodal integration technique in SPFEM, the interpolation of RVEs from the old mesh to the new one is bypassed, which is otherwise infeasible. The smoothing operation in nodal integration further offers a remedy for regularizing mesh dependency in simulation of strain localization problems. Two examples, namely, general failure of a footing and flow of an unstable slope, are used to demonstrate the potential of the proposed method in solving large deformation and providing reliable predictions on collapse and failure of geotechnical problems.

KEYWORDS
footing, large deformation, multiscale modeling, slope failure, SPFEM/DEM

1 | INTRODUCTION

Numerical modeling plays an increasingly important role in geotechnical analysis and design today, and meanwhile, it faces ever growing challenges arising from many aspects of the material behavior and complexity of practical problems. Specifically, geomaterials are composed of discrete particles varying in mineralogical composition, morphology, and size, and exhibit inherent multiscale nature that dictates many macroscopic mechanical responses of these materials. Mathematical formulations of their mechanical behaviors, i.e., constitutive models, have been the backbone for numerical analysis. It remains a formidable task to propose a mathematical model general and robust enough to account for a wide spectrum of material behaviors, ranging from critical state and anisotropy[1,2] to non-coaxiality[3,4] and cyclic hysteresis, and

among other salient features. Meanwhile, modern geotechnical practice has pushed the boundary of geotechnical analysis and design from conventional small strain serviceability to large deformation and even failure. One outstanding example is in offshore geotechnics where soils that bear offshore structures, such as anchors and rigs, have to work in large deformation to provide required bearing capacity. Other examples include the post-failure analysis of a slope and pile penetration into soils[5] where large deformation of soils is a reality. Modeling of large deformation has proven to be challenging for conventional mesh-based numerical methods, such as the finite element method (FEM). Moreover, most available soil models are developed based on small-strain assumption and calibrated by small-to-medium-strain laboratory tests. Their applicability for the large-deformation regime may be questionable.

Over the past four decades, the discrete element method (DEM) has proven to be an effective tool for constitutive modelers and theoreticians to derive material responses from grain assemblies and gain micromechanical insights of material behavior. DEM helps to provide detailed evolution of microstructures (termed fabric) and other state variables of the materials under mechanical loading from small-strain to large-deformation regimes.[6–8] Nevertheless, DEM is believed to best serve as virtual element tests to supplement small-scale laboratory tests. With the constraint of the accessible computing power, it remains impractical in solving engineering-scale problems. Given the challenge in developing sophisticated geomaterial models and the limitation of DEM, a hierarchical multiscale FEM/DEM approach has recently been proposed,[9–13] in which FEM is utilized to solve engineering-scale boundary value problems (BVPs) and the FE Gauss quadrature points are embedded with representative volume elements (RVEs) solved by DEM for the derivation of material constitutive responses. Since the DEM simulation of the RVEs can reproduce complex mechanical behaviors of the geomaterials under various loading paths, the onerous task to develop phenomenological constitutive models is avoided. The approach has been successfully applied in studies of shear failure of geostructures,[14–16] compaction band formation in high-porosity sandstones,[17,18] and coupled thermo-hydro-mechanical problems.[19–22]

Despite all the merits mentioned before, the multiscale FEM/DEM approach is inept at modeling large deformation because of the use of conventional FEM. It hence inevitably suffers from mesh distortion under large deformations, which deteriorates the numerical results and may force the computation to terminate before completion. To meet the challenge of solving large-deformation problems, various remeshing techniques have been proposed, e.g. the remeshing and interpolation technique with small strain (RITSS)[23] and the *rh*-adaptive arbitrary Lagrangian Eulerian (ALE).[24] Besides, many advanced meshfree methods have been developed or adapted from other disciplines for geotechnical engineering applications, such as the smoothed particle hydrodynamics (SPH),[25,26] the material point method (MPM),[27,28] and the peridynamics.[29,30] To enhance the capability of FEM/DEM in modeling large deformation, it is intuitive to seek suitable remeshing techniques for use in the FEM module for the coupled FEM/DEM. However, typical remeshing techniques do not work in a multiscale modeling context, as they require remapping of state variables when a new mesh is generated. In the context of coupled FEM/DEM, it is the physical microstructures represented by the RVEs that have to be interpolated from the old mesh to the new one, which is simply impossible. An alternative solution is to replace FEM with one of those meshfree methods that does not require remapping of state variables or microstructures. For instance, MPM, with all the material information carried by the material points, appears to be a ready candidate. Indeed, some attempts have been made to couple MPM with DEM and its excellence in solving large-deformation geomechanical problems has been demonstrated by examples including granular column collapse, failure of footing foundation, and pipe-soil interaction.[31,32]

This contribution will present another option for multiscale modeling of large-deformation geomechanical problems by replacing the FEM with the smoothed particle FEM (SPFEM)[33–36] to bring new features into multiscale modeling. SPFEM has been developed based on an integration of the particle FEM (PFEM)[37,38] and the smoothed FEM (SFEM).[39] The PFEM discretizes the continuum domain with a set of nodes (or called particles) and employs the Delaunay triangulation for the efficient construction of mesh on the nodes. The nodes will deform with the material following the Lagrangian description and remeshing takes place at a certain interval of loading steps depending on the deformation of the mesh. As remeshing is invoked, the method is capable of modeling large deformations. The PFEM was originally developed to study fluid dynamics problems,[37] and later finds success in the application of a variety of problems, including fluid–structure interaction,[40] non-linear solid mechanics,[41] and coupled multiphysics problems.[42] A state-of-the-art review of the method can be found in [43]. In addition to the PFEM, SPFEM follows the SFEM (the node-based SFEM in particular) using a nodal integration technique originally proposed for meshfree methods,[44] which enables the material state variables to be stored at the nodes instead of the Gauss quadrature points. Consequently, remap of state variables in FEM or PFEM is no longer required in SPFEM, which makes the hierarchical coupling of SPFEM and DEM feasible. It is also worth mentioning that SPFEM possesses several advantages compared with MPM and other meshfree methods. For example, the imposition of essential boundary conditions in MPM or SPH generally requires extra

efforts or workarounds,[45] which is not as straightforward as in SPFEM. In addition, most MPM implementations have adopted an explicit time integration scheme, which may not be as efficient as the implicit scheme when dealing with (quasi-)static problems. Furthermore, SPFEM features a smoothing operation that renders it immune to volumetric locking, even when low-order elements are used.[39] This also makes it less vulnerable to mesh/discretization sensitivity for simulating strain localization problems than conventional FEM or MPM as to be shown in this study. SPFEM has been recently applied to the modeling of large deformations of geomaterials in geotechnical engineering, e.g. in the footing,[33] the landslide,[36] and the column collapse problems.[34] It is noted that in the above studies, a soil constitutive model was necessary to be used with the SPFEM. In the current SPFEM/DEM approach, this phenomenological model can be totally bypassed.

The rest of the paper is organized as follows. The approach and formulation is first introduced in Section 2. Then the implementation of the method is validated in Section 3 with two benchmark tests, before it is applied to the study of large-deformation problems in Section 4, where two demonstrative examples are presented. Finally, the study is concluded in Section 5 with some outlook discussions.

2 | APPROACH AND FORMULATION

The two ingredients of the coupled SPFEM/DEM approach, namely, the SPFEM and the DEM will be briefly introduced in the following. It is noted that SPFEM is a combination of the PFEM[37,38] and the SFEM,[39] which renders the method a variant of the classical FEM, so that most FE formulations apply in SPFEM.

2.1 | Governing equation and FE formulation

The BVP is governed by the balance of momentum equation, which writes:

$$\sigma_{ij,j} + b_i = \rho \ddot{u}_i \tag{1}$$

where σ_{ij} is the stress tensor, b_i is the body force due to gravity, ρ is the density, u_i is the displacement, and a superimposed dot or double-dot denotes the first- or second-order time derivative of the quantity.

For the time integration, the Newmark scheme has been employed[46]

$$\dot{u}_i^{n+1} = \dot{u}_i^n + (1 - \gamma)\Delta t \ddot{u}_i^n + \gamma \Delta t \ddot{u}_i^{n+1} \tag{2}$$

$$u_i^{n+1} = u_i^n + \Delta t \dot{u}_i^n + \left(\frac{1}{2} - \beta\right)\Delta t^2 \ddot{u}_i^n + \beta \Delta t^2 \ddot{u}_i^{n+1} \tag{3}$$

where the superscripts $n + 1$ and n indicate the quantity at two consecutive time steps; Δt is the time step increment; β and γ are two parameters associated with the integration scheme, which is unconditionally stable when $1/2 \leq \gamma \leq 2\beta$. With the aid of the displacement predictor

$$\hat{u}_i^{n+1} = u_i^n + \Delta t \dot{u}_i^n + \left(\frac{1}{2} - \beta\right)\Delta t^2 \ddot{u}_i^n \tag{4}$$

and $\ddot{u}_i^{n+1} = (u_i^{n+1} - \hat{u}_i^{n+1})/(\beta \Delta t^2)$, Eq. (1) can be reformulated as

$$\sigma_{ij,j}^{n+1} + b_i + \tilde{\rho}\hat{u}_i^{n+1} = \tilde{\rho}u_i^{n+1} \tag{5}$$

where $\tilde{\rho} = \rho/(\beta \Delta t^2)$.

The variational form can be obtained by multiplying a test function $\delta \mathbf{u}$ on both sides of Eq. (5) and applying the divergence theorem

$$\int_\Omega \delta\boldsymbol{\varepsilon}^T \boldsymbol{\sigma} \, d\Omega + \int_\Omega \tilde{\rho}(\delta\mathbf{u}^T \cdot \mathbf{u}) \, d\Omega = \int_{\Gamma_t} \delta\mathbf{u}^T \cdot \mathbf{t} \, d\Gamma + \int_\Omega \delta\mathbf{u}^T \cdot \mathbf{b} \, d\Omega + \int_\Omega \tilde{\rho}\delta\mathbf{u}^T \cdot \hat{\mathbf{u}} \, d\Omega \tag{6}$$

where $\delta\boldsymbol{\varepsilon}$ is the gradient of the test function; $\mathbf{t}$ is the traction exerted on the Newmann boundary Γ_t. With a proper discretization function $\mathbf{N}$ so that $\delta\mathbf{u} = \mathbf{N}\delta\mathbf{u}_I$ where the subscript I indicates discrete values defined at FE nodes, the following semi-discrete form can be obtained from Eq. (6) by eliminating $\delta\mathbf{u}_I^T$ on both sides

$$\int_\Omega \mathbf{B}^T \boldsymbol{\sigma} \, d\Omega + \int_\Omega \tilde{\rho}\mathbf{N}^T\mathbf{N} \, d\Omega \, \mathbf{u}_I = \int_{\Gamma_t} \mathbf{N}^T \mathbf{t} \, d\Gamma + \int_\Omega \mathbf{N}^T \mathbf{b} \, d\Omega + \int_\Omega \tilde{\rho}\mathbf{N}^T\mathbf{N} \, d\Omega \, \hat{\mathbf{u}}_I \tag{7}$$

where $\mathbf{B} = \nabla\mathbf{N}$ is the strain-displacement matrix. For the non-linear problem, it is more convenient to reformulate the above equation in the incremental form by iterative schemes with $\boldsymbol{\sigma} \leftarrow \boldsymbol{\sigma}^{\text{old}} + \mathbf{DB}\Delta\mathbf{u}_I$ and $\mathbf{u}_I \leftarrow \mathbf{u}_I^{\text{old}} + \Delta\mathbf{u}_I$, which yields the following compact form (the subscript I has been discarded hereafter for brevity)

$$\mathbf{K}\Delta\mathbf{u} = \mathbf{R} \tag{8}$$

where $\boldsymbol{\sigma}^{\text{old}}$ and $\mathbf{u}^{\text{old}}$ are the stress and the displacement at the previous iteration in the Newton's method; $\mathbf{D}$ is the material tangent modulus; $\Delta\mathbf{u}$ is the nodal displacement increment to be solved for the current iteration; the stiffness matrix $\mathbf{K}$ and the residual force vector $\mathbf{R}$ are expressed as

$$\mathbf{K} = \underbrace{\int_\Omega \mathbf{B}^T\mathbf{DB} \, d\Omega}_{\mathbf{K}_D} + s_d \underbrace{\int_\Omega \tilde{\rho}\mathbf{N}^T\mathbf{N} d\Omega}_{\mathbf{K}_M} \tag{9}$$

$$\mathbf{R} = \underbrace{\int_{\Gamma_t} \mathbf{N}^T \mathbf{t} \, d\Gamma + \int_\Omega \mathbf{N}^T \mathbf{b} \, d\Omega}_{\mathbf{f}^{\text{ext}}} - \underbrace{\int_\Omega \mathbf{B}^T \boldsymbol{\sigma}^{\text{old}} \, d\Omega}_{\mathbf{f}^{\text{int}}} + s_d \mathbf{K}_M(\hat{\mathbf{u}} - \mathbf{u}^{\text{old}}) \tag{10}$$

where $\mathbf{K}_D$ and $\mathbf{K}_M$ denote the material stiffness matrix and the mass matrix, respectively; $\mathbf{f}^{\text{ext}}$ and $\mathbf{f}^{\text{int}}$ are the external and the internal nodal forces, respectively; a flag argument s_d is introduced into the inertia-related terms to differentiate (quasi-)static ($s_d = 0$) or dynamic ($s_d = 1$) cases.

In the dynamic case, the matrix $\mathbf{K}$ could be easily ill-conditioned when the stiffness and the mass matrices have entry values differing in orders of magnitude. It would be more advantageous to adopt an explicit scheme, where Eq. (1) can be written in the following matrix form

$$\mathbf{M}\ddot{\mathbf{u}} = \mathbf{f}^{\text{ext}} - \mathbf{f}^{\text{int}} \tag{11}$$

where

$$\mathbf{M} = \int_\Omega \rho\mathbf{N}^T\mathbf{N} \, d\Omega \tag{12}$$

The mass matrix is usually diagonalized using HRZ-lumping[47] for the ease of computation. In the present SPFEM, the nodal mass is calculated by multiplying the density of the material with the area of the node (for 2D, see Eq. (14)). After finding the acceleration, the velocity and the displacement are updated with the velocity Verlet time integration, which corresponds to a special case of the Newmark scheme with $\gamma = 1/2$ and $\beta = 0$ in Eqs (2) and (3). The velocity Verlet scheme possesses second-order accuracy but is only conditionally stable, so that the time step increment has to be set sufficiently small to satisfy the CFL condition.
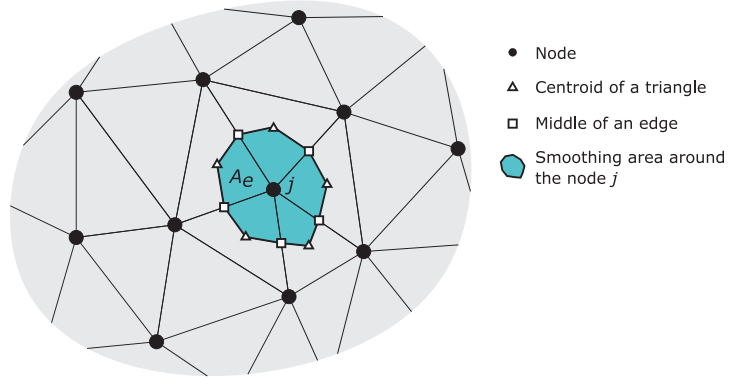
2.2 | SPFEM formulation

SPFEM employs a node-based strain smoothing technique following the smoothed FEM (SFEM, see [39]), where material history-dependent state variables, e.g. the plastic strain in a plasticity model or the microstructure in an RVE model, are associated with nodes instead of Gauss quadrature points as in FEM and PFEM. In the context of SPFEM/DEM approach, it means that the RVEs are attached to the nodes, and the deformation for each RVE is linked to the deformation of the respective node. As a beneficial result, remap of history variables (or RVEs) after remeshing can be averted. Similar to the PFEM, the mesh in SPFEM will be constructed by Delaunay triangulation on the cloud of nodes. Hence, only triangle elements are involved. As illustrated in Figure 1, the smoothing domain of a node is generated by connecting the centroids of triangles and the middle of edges around that node. The smoothed strain-displacement matrix $\tilde{\mathbf{B}}_j$ and the smoothing area A_j at the node j will then be[33–35]

$$\tilde{\mathbf{B}}_j = \frac{1}{A_j} \sum_{e \in \text{sur. tri.}} A_e \mathbf{B}_e \tag{13}$$

$$A_j = \sum_{e \in \text{surr. tri.}} A_e \tag{14}$$

where the summation is over the surrounding triangle elements sharing the same node; A_e and $\mathbf{B}_e$ are the weighting area and the strain-displacement matrix of each triangle, respectively. It is noted that for triangle elements, A_e is 1/3 of the area of each triangle.

The strain at the node j can be evaluated from

$$\varepsilon_j = \tilde{\mathbf{B}}_j \mathbf{u} \tag{15}$$

Accordingly, the material stiffness matrix and the internal force vector in Eqs (9) and (10) will be reformulated by replacing $\mathbf{B}$ with $\tilde{\mathbf{B}}$

$$\mathbf{K}_D = \int_\Omega \tilde{\mathbf{B}}^T \mathbf{D} \tilde{\mathbf{B}} \, d\Omega = \sum_j^{N_j} \tilde{\mathbf{B}}_j^T \mathbf{D}_j \tilde{\mathbf{B}}_j A_j \tag{16}$$

$$\mathbf{f}^{\text{int}} = \int_\Omega \tilde{\mathbf{B}}^T \boldsymbol{\sigma}^0 \, d\Omega = \sum_j^{N_j} \tilde{\mathbf{B}}_j^T \boldsymbol{\sigma}_j^0 A_j \tag{17}$$

where N_j is the total number of nodes in the whole domain.

Another essential element of the SPFEM or PFEM is the application of alpha-shapes[48] to properly identify the domain boundary. PFEM discretizes the problem domain with a set of nodes and applies the Delaunay triangulation to construct the mesh on the nodes. The nodes will displace with the deformation of the material. As a result, PFEM belongs to the Lagrangian approach which has advantages over the Eulerian approach in modeling history-dependent materials

and tracking interfaces in large-deformation problems. However, when remeshing takes place in large deformations, the mesh topology as well as the problem domain may change abruptly. Since a Delaunay triangulation always results in a convex domain, alpha-shapes are commonly used to examine each triangle element and determine if it belongs to the physical domain. Following,[49] a triangle will be deemed as non-physical and removed from the mesh, if its circumradius is greater than αh, where h is the characteristic spacing of the mesh, e.g. the mean length of all the triangle edges; and α is a user-defined parameter and is generally problem-specific but in a typical range of 1.2 to 1.6 for most practical problems.[50]

2.3 | Frictional contact

For simplicity, only contact between a deformable body and a rigid surface is considered, where the former and the latter are treated as the slave and the master boundaries, respectively, for the contact detection. The problem is solved by the penalty method.[51] The normal and the tangential contact forces at a node are calculated as

$$\mathbf{f}_n^{\text{cont}} = -\omega_n\, g_n\, \mathbf{e}_n \tag{18}$$

$$\mathbf{f}_t^{\text{cont}} = \begin{cases} -\omega_t\, g_t\, \mathbf{e}_t, & \text{if } \left|\mathbf{f}_t^{\text{cont}}\right| \leq \mu \left|\mathbf{f}_n^{\text{cont}}\right| \\ \mu\, \omega_n\, g_n\, \text{sign}(g_t)\, \mathbf{e}_t, & \text{otherwise} \end{cases} \tag{19}$$

where ω_n and ω_t are the penalty parameters for the normal and the tangential directions, denoted by $\mathbf{e}_n$ and $\mathbf{e}_t$, respectively; g_n is the penetration depth (contact occurs only if $g_n < 0$); g_t is the accumulated relative tangential displacement at the contact; μ is the frictional coefficient. For the implicit scheme, the contact stiffness is required which is given by

$$\mathbf{k}_n^{\text{cont}} = \omega_n\, \mathbf{e}_n^T \mathbf{e}_n \tag{20}$$

$$\mathbf{k}_t^{\text{cont}} = \begin{cases} \omega_t\, \mathbf{e}_t^T \mathbf{e}_t, & \text{if } \left|\mathbf{f}_t^{\text{cont}}\right| \leq \mu \left|\mathbf{f}_n^{\text{cont}}\right| \\ \mu\, \omega_n\, \text{sign}(g_t)\, \mathbf{e}_t^T \mathbf{e}_n, & \text{otherwise} \end{cases} \tag{21}$$

The contact stiffness matrix and the contact force will be included in the governing equation

$$\mathbf{K} = \mathbf{K}_D + s_d \mathbf{K}_M + \mathbf{K}_C \tag{22}$$

$$\mathbf{R} = \mathbf{f}^{\text{ext}} - \mathbf{f}^{\text{int}} + \mathbf{f}^{\text{cont}} + s_d \mathbf{K}_M(\hat{\mathbf{u}} - \mathbf{u}^0) \tag{23}$$

where the global contact stiffness matrix $\mathbf{K}_C$ and the contact force vector $\mathbf{f}^{\text{cont}}$ are assembled from all the nodes in the domain

$$\mathbf{K}_C = \sum_{N_j} \left(\mathbf{k}_n^{\text{cont}} + \mathbf{k}_t^{\text{cont}}\right) \tag{24}$$

$$\mathbf{f}^{\text{cont}} = \sum_{N_j} \left(\mathbf{f}_n^{\text{cont}} + \mathbf{f}_t^{\text{cont}}\right) \tag{25}$$

For the explicit scheme, Eq. (11) will also include the contact force term

$$\mathbf{M}\ddot{\mathbf{u}} = \mathbf{f}^{\text{ext}} - \mathbf{f}^{\text{int}} + \mathbf{f}^{\text{cont}} \tag{26}$$

2.4 | DEM model

For the DEM module, a popular open-source code YADE[52] has been used, where 2D simulations on the RVE packings with circular particles and periodic boundaries were performed to qualitatively approximate the plane-strain behavior of sands. Whereas 2D simulations have been adopted in the study to minimize the computational cost, the framework is equally applicable to 3D scenarios (see [18, 53]). In the DEM model, the inter-particle contact is described by a simple linear force-displacement law, in conjunction with the Coulomb friction. The normal stiffness k_n and the tangential stiffness k_t are calculated as:

$$\begin{cases} k_n = E_c\, r^* \\ k_t = \nu_c\, k_n \end{cases} \tag{27}$$

where E_c and ν_c are two user-defined parameters; $r^* = 2r_1 r_2/(r_1 + r_2)$ is the common radius of the two particles (with radii r_1 and r_2, respectively) in contact. To model cohesive granular materials, all the existing contacts are assigned with a contact bond, the strength of which is given by $c \times \min(r_1, r_2)^2$, where c is a cohesion strength parameter.[17] The contact bonds permit the transmission of tensile forces at the contacts, but no moments as opposed to the parallel bonds,[54] and will break permanently once either the tensile force or the shear force exceeds a certain threshold, leaving a purely frictional contact. Other typical DEM input parameters include the inter-particle contact friction angle φ, the damping ratio λ and the particle density ρ_p. These parameters are self-explanatory and will not be discussed in detail to avoid distraction of the presentation. Interested readers are referred to the YADE manual.[52]

In the multiscale approach, the boundary conditions for the local RVE packings are prescribed by the displacement gradients $u_{i,j}$ according to the SPFEM solution. After the DEM computation on the RVE packings, two macroscopic quantities, the Cauchy stress σ_{ij} and the tangent modulus D_{ijkl} are extracted via homogenization, and returned to SPFEM (i.e. to formulate Eqs (16) and (17)) to complete the computation cycle. The homogenization is given by[55]

$$\sigma_{ij} = \frac{1}{V} \sum_c^{N_c} d_i^c f_j^c \tag{28}$$

$$D_{ijkl} = \frac{1}{V} \sum_c^{N_c} \left(k_n n_i^c d_j^c n_k^c d_l^c + k_t t_i^c d_j^c t_k^c d_l^c \right) \tag{29}$$

where V is the volume of the RVE packing, N_c is the total number of contacts, d_i^c is the branch vector connecting the centroids of the two particles in contact, f_i^c is the contact force, n_i^c and t_i^c are the unit vectors along the normal and the tangential directions at a contact, respectively. It is noteworthy that the tangent operator D_{ijkl} is derived from the RVE packing by assuming a uniform strain within the packing[55] and is only required by the implicit scheme using Eq. (8), but unnecessary for the explicit scheme using Eq. (11). Another point worth mentioning is that the deformation described by the displacement gradient contains both strain and rotation, and the homogenized stress from Eq. (28) is corotational and objective. Hence, it is needless to resort to other stress rate measures such as the Jaumann rate.[19]

For the presentation of results, the mean stress p (compressive stress and strain treated as positive following the convention in soil mechanics) and the deviatoric stress q are defined (for 2D):
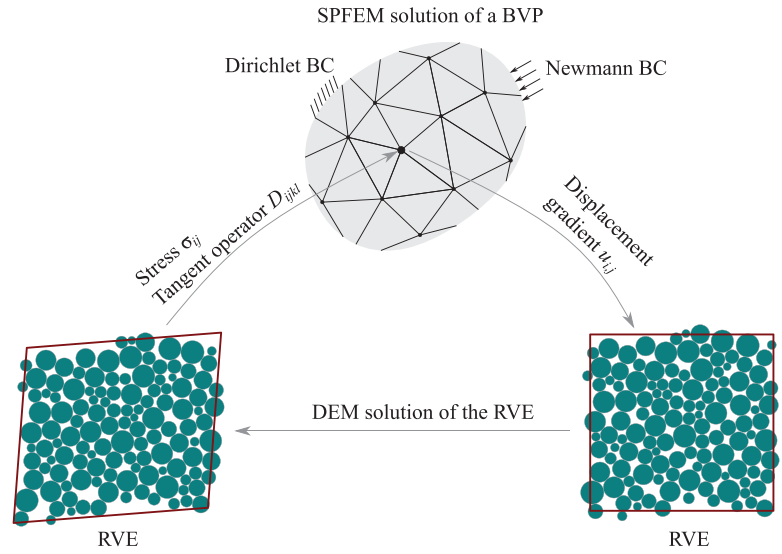
$$p = -\frac{1}{2}\sigma_{ii} \tag{30}$$

$$q = \sqrt{\frac{1}{2}s_{ij}s_{ij}} \tag{31}$$

where s_{ij} is the deviatoric part of the stress tensor. Similarly, the two strain measures, the volumetric strain ε_v and the deviatoric strain ε_q, are given by

$$\varepsilon_v = -\varepsilon_{ii} \tag{32}$$

$$\varepsilon_q = \sqrt{2e_{ij}e_{ij}} \tag{33}$$

where the strain tensor ε_{ij} is the symmetric part of the displacement gradient $u_{i,j}$; and e_{ij} is the deviatoric part of ε_{ij}.

2.5 | Coupling and computational procedure

The coupling between the SPFEM and the DEM is realized in the way that when the global governing equation is solved by the SPFEM, the method will resort to the DEM for the stress update at the nodes. The coupling procedure for the SPFEM/DEM computation is illustrated in Figure 2 and summarized below:

(i) Discretize the domain with a cloud of nodes; attach RVEs to each node with a given initial condition;
(ii) Construct the mesh on the nodes using Delaunay triangulation with a suitable computational geometry library, e.g. `CGAL`[56] has been used in this study;
(iii) Invoke alpha-shapes to identify boundaries and remove non-physical elements;
(iv) Solve the governing equation with SPFEM; for the explicit scheme, find the solution of Eq. (11) directly and move to step (v); for the implicit scheme, use the Newton's method to tackle non-linearity of Eq. (8):
   (a) Find a trial solution;
   (b) Apply the displacement gradients at the nodes as the boundary condition on each RVE and solve the RVE with DEM to update the stiffness and the stress;
   (c) Update the frictional contact force and the stiffness, if there is any, the global stiffness matrix and the residual force vector;
   (d) Update the solution and determine if convergence has been reached; if not, return back to substep (a).
(v) Update the nodal positions, the RVEs attached to the nodes, and the boundary conditions; move to step (ii) for the next loading step until all the steps are finished.

3 | VALIDATION

The implementation of the SPFEM and the coupled SPFEM/DEM has been first validated by two classical problems, namely, the sliding block test and the biaxial shear test. As the two tests are either static or quasi-static, the implicit approach proves to be a better option, and the inertia-related terms in Eqs (9) and (10) can be omitted in the computation by setting $s_d = 0$.

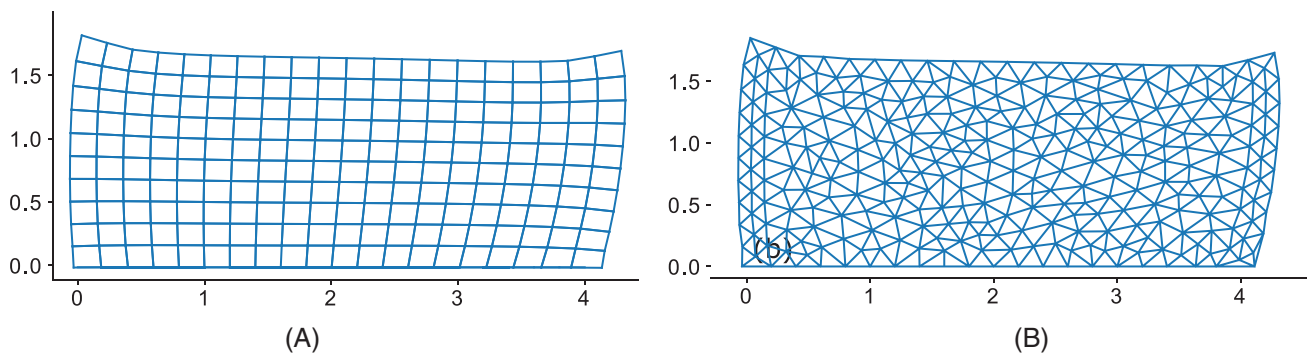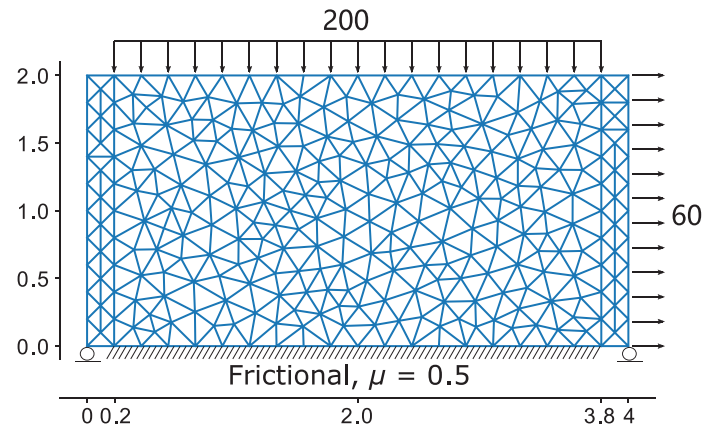**FIGURE 3** Mesh and boundary conditions for the sliding block test.

FIGURE 4 Deformed mesh for the sliding block test: (a) FEM solution, and (b) SPFEM solution.

3.1 | Sliding block test

The sliding block test is a conventional benchmark test for frictional interface problems where a plane strain elastic block is pulled to deform on a rigid frictional surface. The problem was first analyzed by[57] and later referenced by some subsequent studies.[58,59] The size of the block is 4 units in length and 2 units in height. The material is elastic with a Young's modulus of 1000 units and a Poisson's ratio of 0.3. The block is resting on a horizontal surface roughened in a coordinate range from 0.2 to 3.8 with a frictional coefficient $\mu = 0.5$, and the two corners are supported by rollers. On the top surface in the same range, a uniformly distributed compressive pressure of 200 units is applied. The right surface of the block is subjected to a pulling traction of 60 units. No gravity is considered. The dimension, the boundary condition, as well as the mesh to be used by SPFEM are illustrated in Figure 3, where the random unstructured mesh was generated by Gmsh.[60]

The deformed shape of the block subjected to the prescribed loading is shown in Figure 4, where an FEM solution using Escript[61] with contact elements is also provided for comparison. Figure 5 presents the normal and the shear traction along the frictional surface. It is seen that the results from the present FEM and SPFEM solutions are in good agreement with those obtained from the literature.[57–59] It is also interesting to find that the shear traction changes from positive to negative at a coordinate around 1.2, suggesting a complicated deformation pattern of the elastic body under the compound loading conditions.

3.2 | Biaxial shear test

The proceeding sliding block test has been devoted to the validation of the implementation of SPFEM. The coupling between SPFEM and DEM will be examined in this subsection by the biaxial shear test. A number of biaxial shear tests have been done previously using FEM/DEM.[10,62] The results will be used for comparison with the present study.

The first step in a multiscale analysis is the preparation of a proper RVE. Following the previous studies,[10] the RVE consists of 400 cohesionless circular particles with their radii ranging from 3 mm to 7 mm. The parameters for the DEM

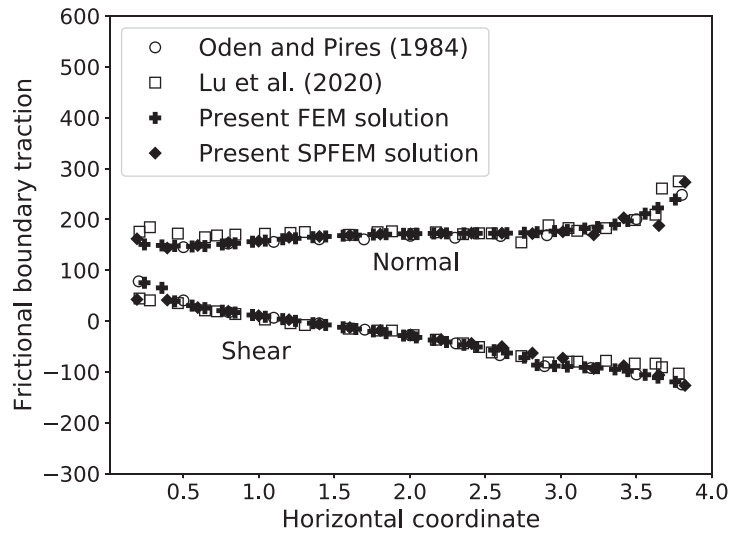**FIGURE 5** Boundary traction along the frictional contact surface.

TABLE 1 DEM model parameters for the biaxial shear test

Radius (mm)	ρ_p (kg/m³)	E_c (MPa)	ν_c	c (kPa)	φ (rad)	λ
3–7	2650	800	0.8	0	0.5	0.1

model are summarized in Table 1. The RVE was isotropically consolidated to a mean stress level of $p_0 = 100$ kPa and an initial void ratio of $e_0 = 0.178$ prior to be embedded to each of the nodes in SPFEM (or Gauss points in FEM). The prepared RVE is shown in Figure 6, on which the force chains are superimposed and represented by line segments with their widths proportional to the magnitudes of the normal contact forces.

The sand specimen has a dimension of 0.05 m in width and 0.1 m in height. It is supported by rollers at the flat bottom, which is only fixed at the center to prevent rigid body motion. The two lateral surfaces are subjected to a confining pressure of 100 kPa. Incremental vertical displacements are prescribed on the top surface to load the specimen, where horizontal movements are allowed (i.e. smooth boundary). Gravity is also ignored. To investigate the effect of mesh sensitivity, three meshes with different densities are considered and illustrated in Figure 7. The coarse one has a total of 80 nodes and 129 triangle elements, the medium-fine one 288 nodes and 516 triangle elements, and the fine one 612 nodes and 1134 triangle elements. It is noted that the topology of the meshes remains unchanged in FEM/DEM simulations but may alter in SPFEM/DEM due to the mesh reconstruction process activated in the latter approach.

The global axial stress-strain responses from the simulations are collectively shown in Figure 8, where the nominal axial stress is defined as the resultant axial force divided by the width of the specimen, and the nominal axial strain is the vertical displacement normalized by the original height. The RVE response from a separate pure DEM biaxial shear test on the RVE is also presented in the figure, which can be seen as the constitutive response of the material. A typical
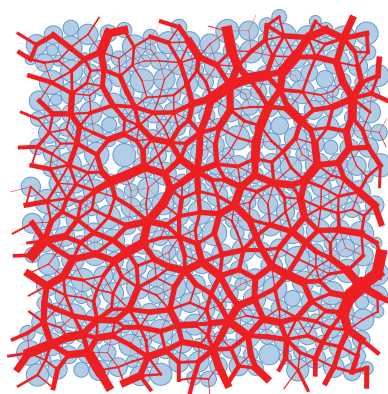

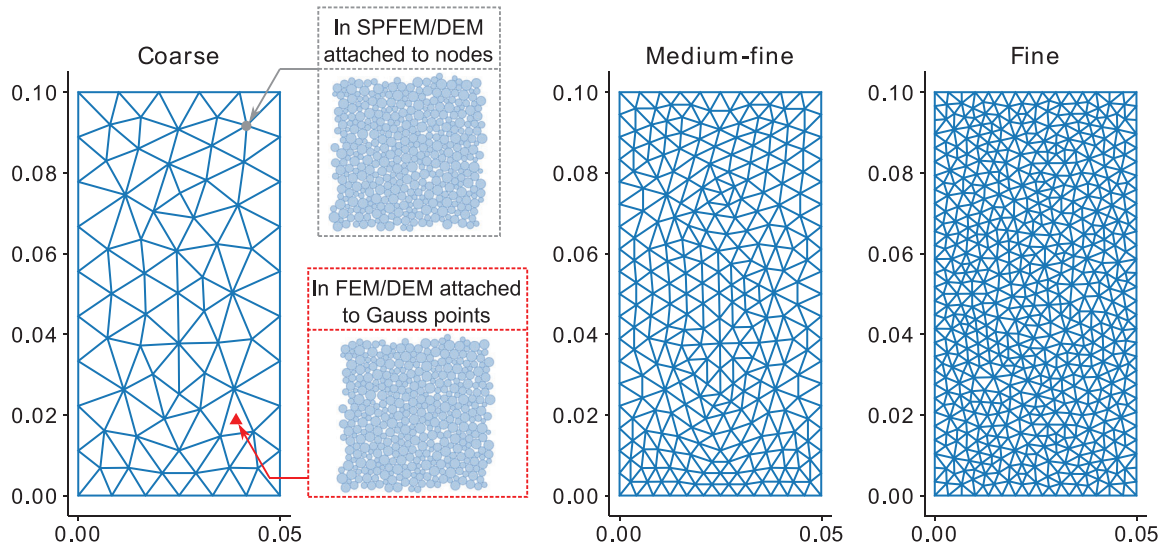**FIGURE 6** RVE packing after isotropic consolidation for the biaxial shear test.

FIGURE 7 Coarse, medium-fine and fine meshes for the biaxial shear test. The inset shows that the RVEs are attached to the nodes in SPFEM/DEM and the Gauss points in FEM/DEM.

FIGURE 8 Nominal axial stress-strain responses of the biaxial shear test predicted by FEM/DEM and SPFEM/DEM using three different meshes.
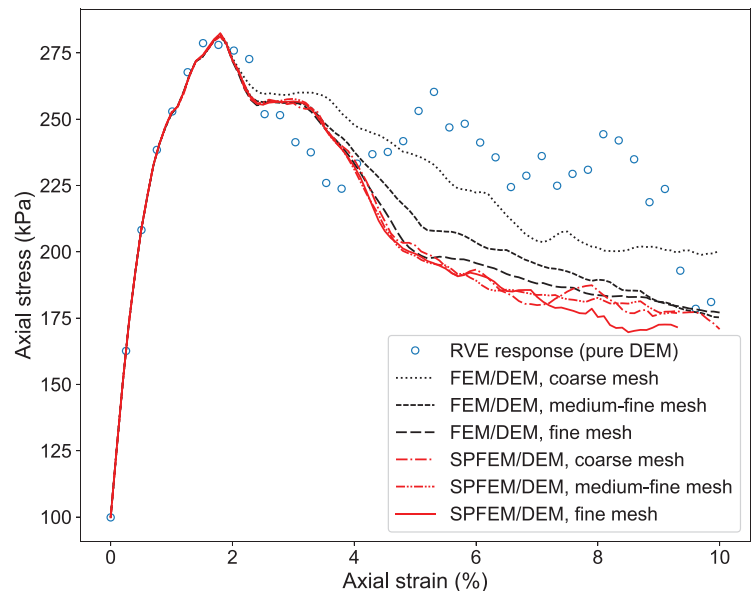
strain softening behavior for dense sands under biaxial shear has been observed in all the cases. It is found that all the curves reach a same peak stress of about 280 kPa at a strain level of 1.8% and their pre-peak behaviors are almost identical to that of the RVE response, though their post-peak responses deviate from each other. Albeit the strong fluctuations in the RVE post-peak response, the global responses from the coupled simulations are relatively smooth and generally have smaller post-peak strengths due to the occurrence of strain localization within the specimen, which will be discussed later. In addition, as has been demonstrated in previous studies, the use of a finer mesh yields a softer post-peak response in FEM/DEM simulations.[10] Nevertheless, the present SPFEM/DEM study shows that the method is less prone to the mesh size dependency as the three post-peak curves using the coarse to fine meshes are quite close and are generally lower than the FEM/DEM results. The relative mesh insensitivity of the SPFEM/DEM approach is probably attributable to the smoothing operation applied in the approach. As the FEM/DEM result gets closer to the SPFEM/DEM result when the mesh is refined, it is reasonably concluded that the SPFEM/DEM will predict better results than the FEM/DEM given a same mesh.

The shear deformation within the specimen is presented in Figure 9 in terms of the deviatoric strain contour at an axial strain level of 9%. Strain localization is clearly observable in all the simulation cases where a single shear band takes place
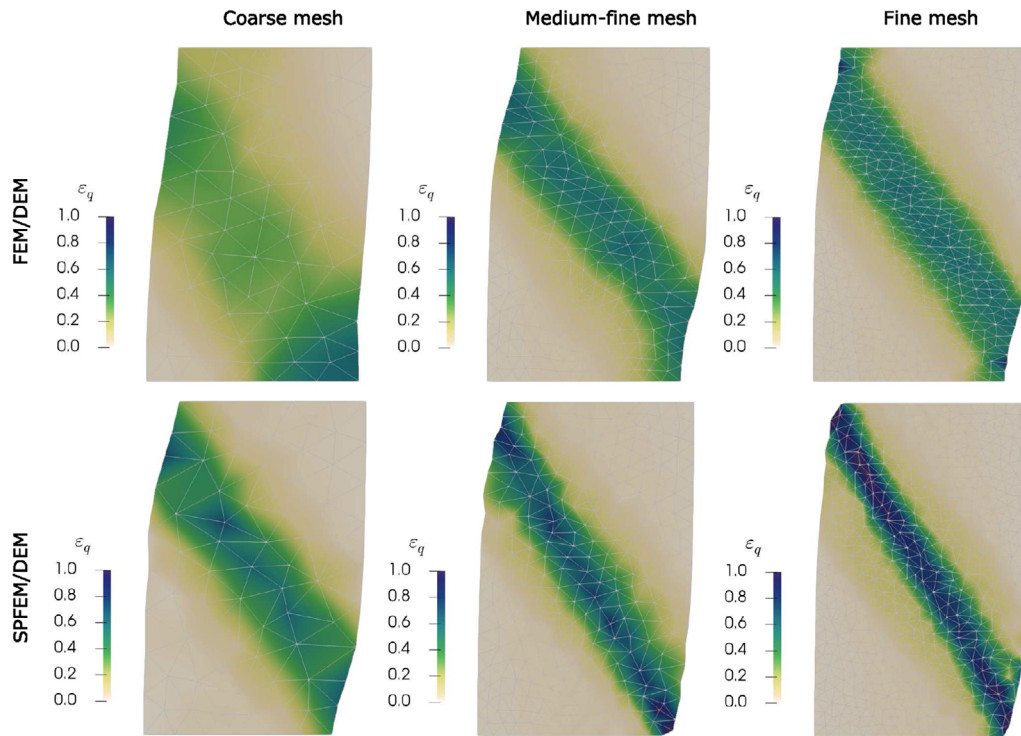
FIGURE 9 Contour of the deviatoric strain at 9% nominal axial strain.

TABLE 2 DEM model parameters for the footing problem

Radius (mm)	ρ_p (kg/m³)	E_c (MPa)	ν_c	c (kPa)	φ (rad)	λ
3–7	2650	600	0.8	100	0.5	0.1

in the specimen. However with FEM/DEM, the width of shear band is apparently dependent on the mesh size — a finer mesh leads to a thinner shear band and more concentrated strain localization. In contrast, the SPFEM/DEM results using the three meshes show a similar shear band width, which is consistent with the stress-strain results shown in Figure 8, and is indicative of the capability of SPFEM in regularizing the solution for strain localization problems.

4 | LARGE-DEFORMATION GEOMECHANICAL PROBLEMS

The competence of the SPFEM/DEM approach in solving large-deformation geomechanical problems is demonstrated in this section with the following two examples.

4.1 | General failure of footing

The study of the bearing capacity of a footing and its failure pattern is classical in geotechnical engineering. This example analyzes a rigid strip footing driven vertically into a cohesionless soil. The base of the footing is assumed to be perfectly rough. Only half of the domain is treated by assuming symmetry of the problem. The size of the half domain is 5 m in both width and depth. The half width of the footing is $B = 0.5$ m. There is no surcharge applied on the surface but gravity is included in the simulation which yields a stress level ranging from 0 to 100 kPa within the domain (the bulk unit weight of the soil is taken as $\gamma_w = 20$ kN/m³). The microscopic parameters used in the RVE (with 400 circular particles) are listed in Table 2. A small inter-particle cohesion was introduced to stabilize the packing at low stress levels. For reference, the constitutive responses of the RVE subjected to the biaxial shear test are shown in Figure 10 considering three different confining pressure levels in the same range as in the footing problem. It is seen that the soil is generally dilative and a
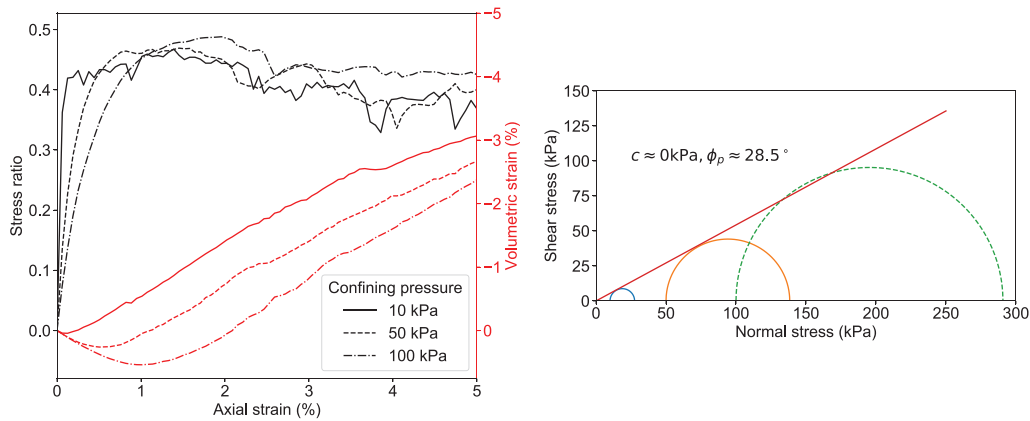
FIGURE 10 Drained biaxial shear responses of the RVE assigned to the footing problem under different confining pressure levels and the corresponding Mohr's circles at their peak stress states.
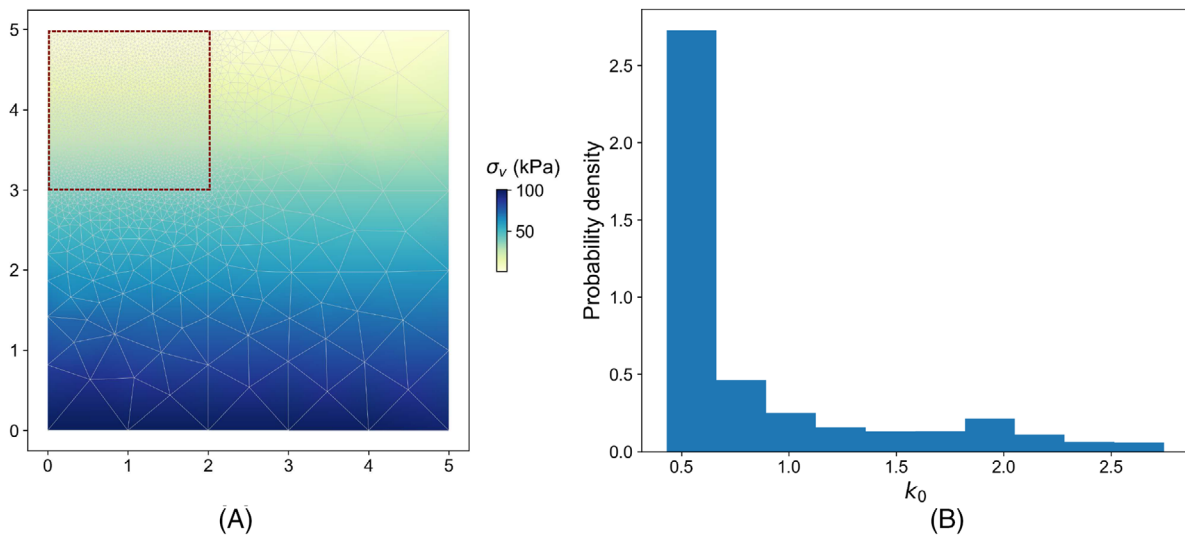

FIGURE 11 (a) In-situ vertical stress profile (the dashed square indicates the region where alpha shapes are applied); (b) Probability density of the coefficient of earth pressure at rest.

small softening response has been observed. From their Mohr's circles at the peak stress states, it is estimated that the cohesion of the soil is negligible and its peak friction angle ϕ_p is approximately 28.5° (note that the two circles with small stress levels are used for the fitting as they are more relevant in the shallow footing problem).

The in-situ stress state of the soil is prepared by allowing the soil to settle under gravity. During this phase of computation, the horizontal degrees of freedom (DOFs) of the nodes on the two vertical sides and the vertical DOFs of the nodes on the bottom side are restricted. The initial RVE was isotropically consolidated to $p_0 = 10$ kPa and $e_0 = 0.192$ before assigned to the nodes of the entire domain. The profile of the vertical stress σ_v after equilibrium is presented in Figure 11, along with the distribution of the coefficient of earth pressure at rest k_0. It is found that k_0 is largely around 0.5 ($\approx 1 - \sin\phi_p$) within the whole domain, and the few deviations are located at the surface of the domain where the stress level is close to 0. The initial mesh used in the simulation can also be seen from Figure 11(a), which contains 2690 nodes and 5268 triangle elements. Note that as a non-uniform mesh is used, alpha shapes are applied only to the region around the footing as indicated by the dashed square in the figure. After equilibrium is reached, the footing is pushed downwards to mobilize its bearing capacity and to trigger failure of the foundation eventually. Since the problem is quasi-static, the implicit scheme has been used with the flag parameter s_d set to 0.

The evolution curves of the resultant vertical stress on the footing from SPFEM/DEM and FEM/DEM simulations are collectively plotted in Figure 12. Additional results using a coarse mesh (800 nodes and 1532 triangle elements) are supplemented to examine the mesh sensitivity of the two approaches. The ultimate bearing capacity of a shallow footing
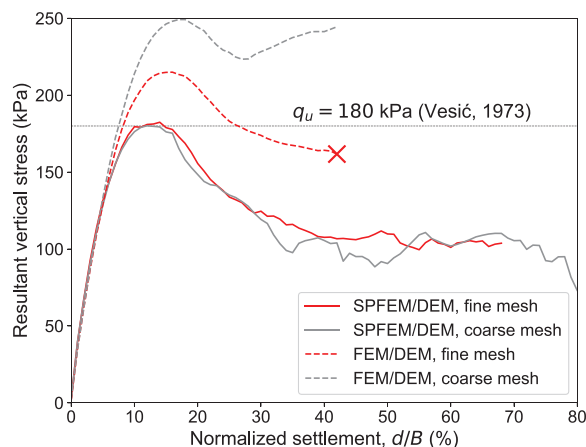
FIGURE 12 Evolution of the resultant vertical stress on the footing. The cross marker × indicates where program aborts due to mesh tangling.
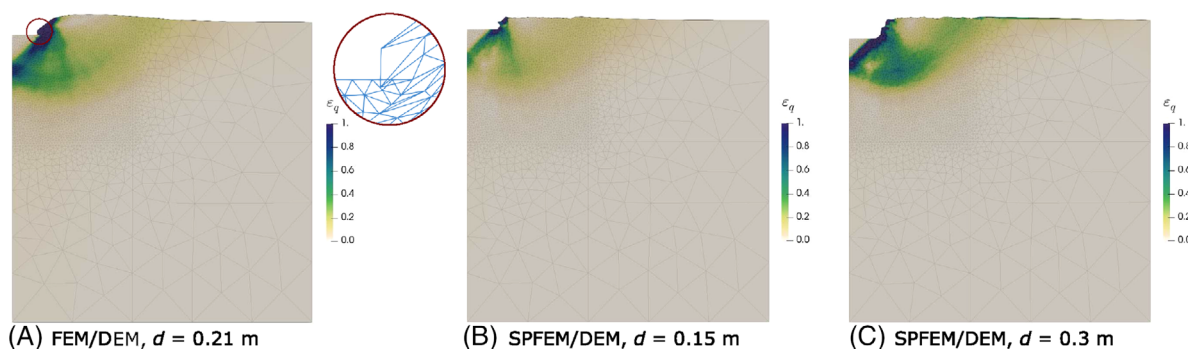

FIGURE 13 Deformation field of the foundation simulated by (a) FEM/DEM at $d = 0.21$ m; (b) SPFEM/DEM at $d = 0.15$ m; and (c) SPFEM/DEM at $d = 0.3$ m. The inset in (a) is a zoomed plot of the region with notable mesh tangling.

under general failure can be estimated using the Terzaghi's equation $q_u = \gamma_w B N_\gamma$ (note that B is the half width of the footing) in the absence of cohesion and surcharge. The bearing capacity factor N_γ is a function of the soil friction angle, but its determination varies significantly according to different methods. The value provided in [63] is followed here, i.e. $N_\gamma = 18$ from interpolation when the soil friction angle is 28.5°. Therefore, the ultimate bearing capacity is estimated to be $q_u = 180$ kPa. From Figure 12, it is encouraging to see that SPFEM/DEM predicts very close values to the Vesić's result and the prediction is evidently mesh insensitive. On the contrary, FEM/DEM gives much larger predictions on the bearing capacity than SPFEM/DEM, and its results show clearly mesh dependency — a finer mesh yields a lower prediction. It is reasonably expected that the FEM/DEM prediction will continue decreasing with further mesh refinement and get closer to the SPFEM/DEM prediction eventually. These findings are consistent with that from the biaxial shear test in Section 3.2 (i.e. Figure 8), corroborating the ability of SPFEM/DEM to remedy mesh dependency in strain localization problems. Albeit the merit, severe deterioration of the mesh quality is observed in SPFEM/DEM after $d/B = 70\%$ (where d is the footing settlement), which renders the simulation results afterwards less reliable. For improvement, it is suggested to further refine the mesh which, however, will not be attempted in the study due to the limit of accessible computing resources.

The deformation fields simulated by the two approaches are selectively shown in Figure 13 in terms of the deviatoric strain contours. It is noted that the FEM/DEM simulation was terminated at $d = 0.21$ m caused by mesh tangling. Its deformation field at this stage is shown in Figure 13(a), where a general failure pattern can be roughly identified, i.e. the failure zone is composed of an inverted triangle wedge, a thick spiral slip curve propagating from the lower vertex of the wedge up to the surface of the foundation, and some tributary shear bands between the footing edge and the spiral curve. The local mesh tangling can be clearly seen from the zoomed plot. The simulation results of SPFEM/DEM at two levels of settlement are shown in Figure 13(b–c). The deformation pattern is in general similar to that given by FEM/DEM, and mesh tangling can be effectively avoided in SPFEM/DEM even at large deformations.
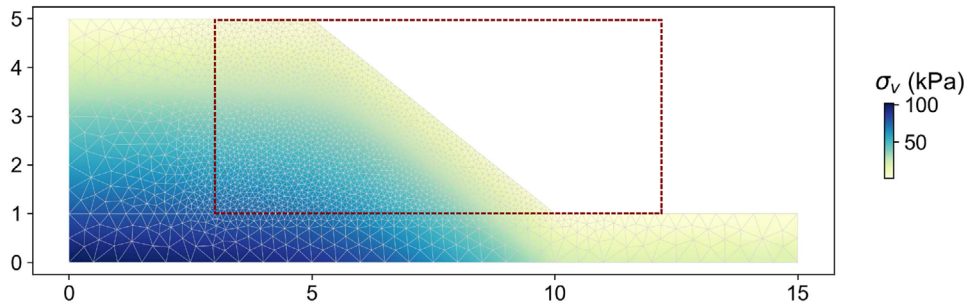
FIGURE 14 In-situ vertical stress profile of the slope (the dashed rectangle indicates the region where alpha shapes are applied).
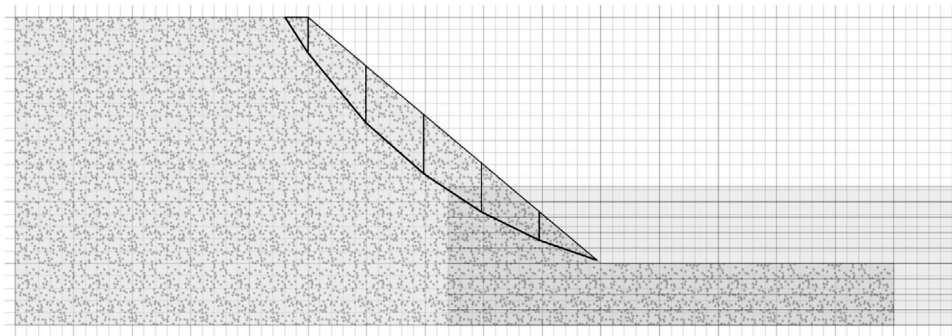

FIGURE 15 Slip surface predicted by the Bishop method. The determined factor of safety of the slope is 0.826.

Finally, it is worth mentioning that since the number of nodes is only about half of the number of elements in a typical 2D Delaunay triangulation, the SPFEM/DEM approach involves much less RVEs and is thus more computationally efficient than the FEM/DEM approach with the same discretization.

4.2 | Slope failure

The post-failure deformation of a slope is crucially important for related risk assessment and hazard mitigation. In this example, the SPFEM/DEM approach will be employed to study the flow behavior of an initially unstable slope. The geometry of the slope is shown in Figure 14, where its dimension is presented as 4 m in height and 4:5 in slope angle. The initial mesh for this problem has 2135 nodes and 4127 triangle elements. The soil properties are the same as that in the footing problem, i.e. the same RVE parameters as in Table 2 and the bulk unit weight of 20 kN/m^3. The initial stress state of the slope is prepared by allowing the soil to settle under gravity as well, but all the nodes in the domain except the ones on the bottom, which are fixed in both directions, only have vertical DOFs considering the special geometry. The distribution of k_0 is found similar to that in Figure 11(b) because of the same protocol applied in generating the initial stress state. After the preparation of the in-situ state, the horizontal DOFs of the nodes other than that on the bottom and the two vertical sides (the three boundaries are fixed in space) will be released on the second phase of computation. Given that the internal friction angle of an RVE packing with round particles is typically smaller than 4/5 (see Figure 10) and the cohesion is negligible, the slope is regarded as unstable and expected to fail under gravity. This problem is dynamic and solved by the implicit scheme with s_d switched to 1. The implicit scheme allows us to use a relatively large time step size, which is chosen as $\Delta t = 10^{-3}$ s.

For comparison, limit equilibrium analysis was first conducted using the Bishop method available in the freeware D-Stability.[64] The soil properties are assigned as close as possible to that in the study: the bulk unit weight 20 kN/m^3, the friction angle 28.5°, the cohesion 1 kPa, and the dilation angle 0°. Note that a small cohesion is introduced. Otherwise, it will result in a surface failure of the slope. The influence of the dilation angle on the slip surface is found negligible, but increasing the dilation angle from 0° to 30° will increase the factor of safety from 0.826 to 0.94. The slip surface predicted by the Bishop method is shown in Figure 15, which starts from the toe and propagates towards the top surface near the crest of the slope.
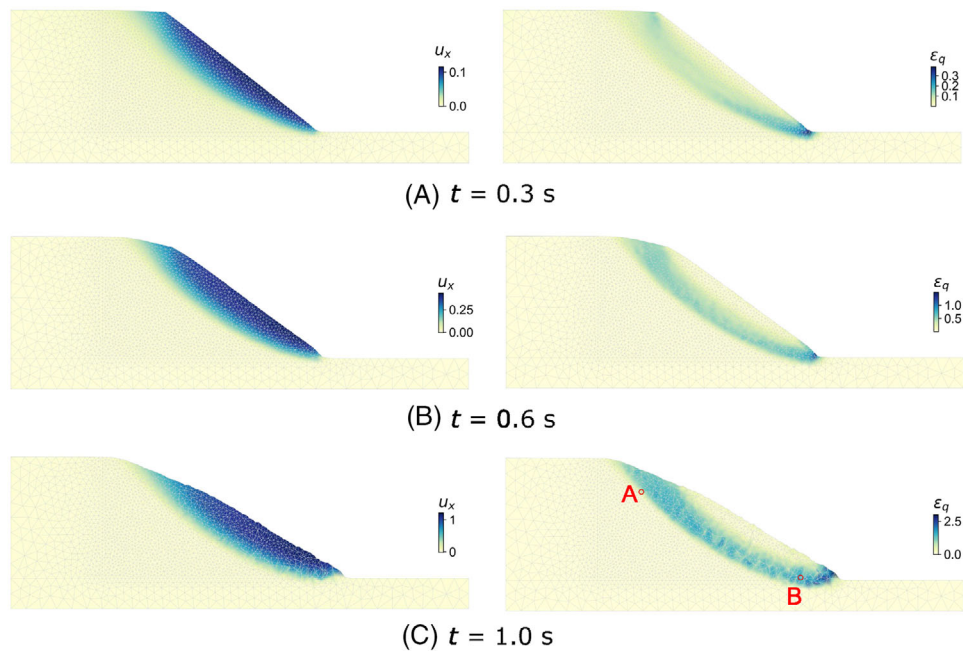
FIGURE 16 Horizontal displacement and deviatoric strain contours at (a) $t = 0.3$ s, (b) $t = 0.6$ s, and (c) $t = 1$ s.

The complete process of the failure initiation and the post-failure flow can be well modeled by the SPFEM/DEM. The contours of the horizontal displacement u_x and the deviatoric strain ε_q at three time instants are shown in Figure 16. At the early stage ($t = 0.3$ s), a slip surface penetrating through the slope is clearly observable from the two contours, which agrees fairly well with that predicted by the Bishop method. However, as time evolves, a progressive failure is observed. The slip surface shifts leftwards, and more soil mass slips down and deposits at the base. At $t = 1$ s, the maximum runout distance is around 1.2 m.

From the contours of the deviatoric strain, it is seen that large shear localization or shear banding happens at the slip surface. The deformation level can reach as high as 100% inside the shear band at $t = 0.6$ s and 1 s. Especially the locations close to the toe have undergone extremely large shear deformation ($\varepsilon_q > 300\%$ at $t = 1$ s). The RVEs associated with the two nodes marked in Figure 16(c) are picked up to show the changes of their microstructures in Figure 17. As the two nodes have a similar initial burial depth, their initial stress states are close to each other, so are the two RVEs at $t = 0$ s. The contact normal distribution in the rose diagram shows moderate anisotropy (the shape of the dashed gray lines deviates moderately from a circle). At the final state ($t = 1$ s), both nodes have experienced large deformation and rotation, but reveals different deformation modes. The mode for Node A is more similar to a biaxial shear, accompanied with rigid body rotation. The contact normal distribution at $t = 1$ s shows large anisotropy, with the major principal direction aligned vertically (solid red lines). In contrast, the mode for Node B exactly resembles a simple shear. The major principal direction of its contact normal distribution matches that of a simple shear at around 120°.

5 | CONCLUSIONS

The study has presented an extension to the multiscale FEM/DEM approach previously developed by the authors by replacing FEM with SPFEM, aiming to solve large-deformation geomechanical problems. The approach features a hierarchical coupling of SPFEM and DEM, in which the former is used to discretize the problem domain and to solve the governing equations, whereas the latter is employed to derive the material constitutive relations by solving local RVEs embedded at the SPFEM nodes. Since SPFEM is essentially a combination of PFEM and SFEM, it inherits some merits of both methods. The major inherited benefits, which make the coupled approach suitable for the purpose of the study, include the capabilities to model large deformations through remeshing and to bypass interpolation of state variables with the nodal integration technique. The approach has been validated first and then applied to the study of two classical geomechanical problems. The key findings from the study are summarized below.
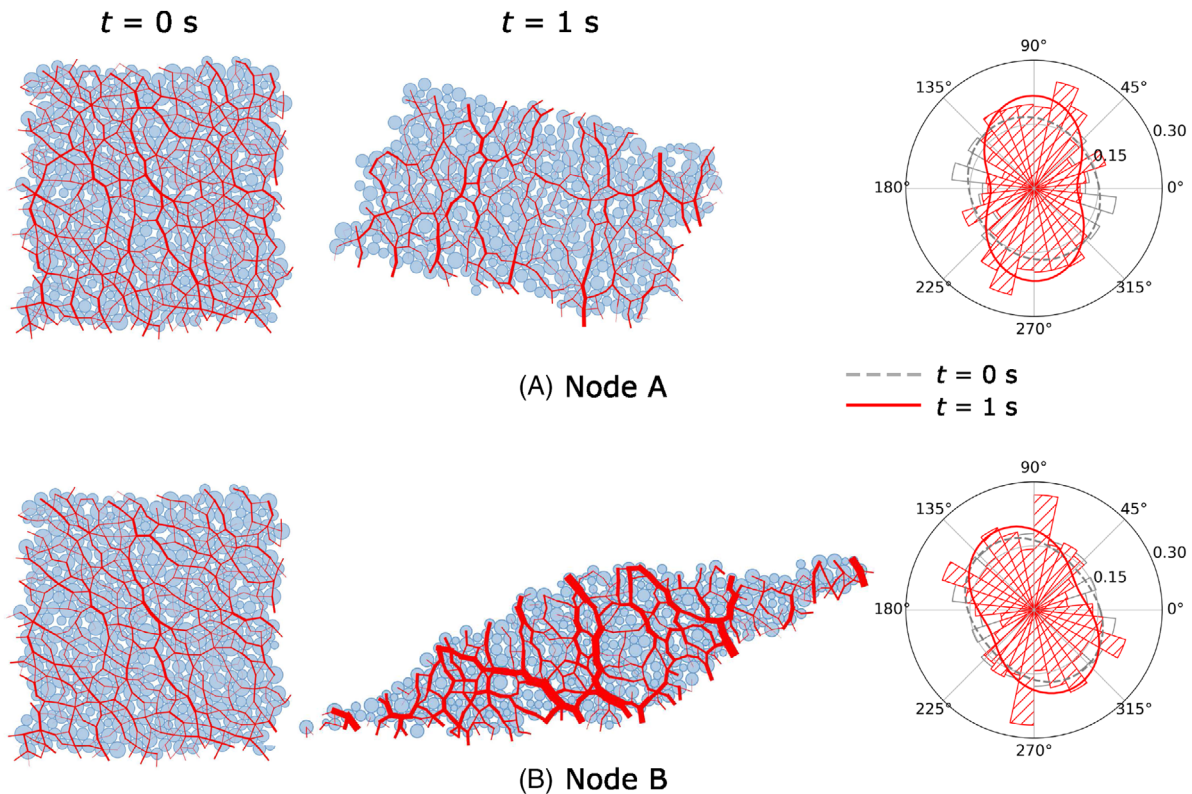
FIGURE 17 The initial ($t = 0$ s) and the final ($t = 1$ s) microstructures at the two selected locations, reflected by the attached RVEs.

(1) An integrated framework is formulated, which can solve both (quasi-)static and dynamic problems using either the implicit or the explicit scheme.
(2) Similar as FEM/DEM, SPFEM/DEM does not require presumed phenomenological constitutive models, and can provide micromechanical insights to macroscopic observations such as failure of geostructures involving strain localization.
(3) Compared with FEM, SPFEM is able to yield mesh insensitive results in strain localization problems due to its smoothing operation.
(4) With the same discretization, SPFEM/DEM is more computationally efficient than FEM/DEM as the number of nodes is only about half of the number of elements in a typical 2D Delaunay triangulation. Hence, SPFEM/DEM involves much less RVEs than FEM/DEM.
(5) The predictions of the bearing capacity of a footing and the slip surface of an unstable slope made by SPFEM/DEM possess satisfactory accuracy with reference to the limit equilibrium analyses.

The approach, however, is not without limitations. First, it is better suited for problems with free surfaces, as surface tracking is difficult with frequent remeshing. Second, while relatively coarse meshes have been adopted in the study due to the limited accessible computing power, fine meshes are required for most large-deformation problems as the spacing of nodes can change abruptly in these scenarios, which on the other hand will impose a large computational burden on the approach. On the bright side, the approach fits perfectly well for parallel computing, with its hierarchical structure closely conforming with the divide-and-conquer strategy (i.e. the domain is divided into non-interactive RVEs that can be solved individually). The alleviation of the multiscale computation by MPI or GPU technologies is demonstrated elsewhere,[13,19 65] which shows the prospects of the approach in solving engineering-scale problems.

ORCID

Ning Guo 🆔 https://orcid.org/0000-0002-5515-9911
Zhongxuan Yang 🆔 https://orcid.org/0000-0003-4632-1355
Weihai Yuan 🆔 https://orcid.org/0000-0002-0732-4329
Jidong Zhao 🆔 https://orcid.org/0000-0002-6344-638X

REFERENCES

1. Li XS, Dafalias YF. Anisotropic critical state theory: Role of fabric. *Journal of Engineering Mechanics*. 2012;138:263–275.
2. Yang Z, Liao D, Xu T. A hypoplastic model for granular soils incorporating anisotropic critical state theory. *International Journal for Numerical and Analytical Methods in Geomechanics*. 2020;44:723–748.
3. Wu QX, Yang ZX, Li X. Numerical simulations of granular material behavior under rotation of principal stresses: micromechanical observation and energy consideration. *Meccanica*. 2019;54:723–740.
4. Li XS, Dafalias YF. Noncoaxiality between two tensors with application to stress rate decomposition and fabric anisotropy variable. *Journal of Engineering Mechanics*. 2020;146:04020004.
5. Yang ZX, Gao YY, Jardine RJ, Guo WB, Wang D. Large deformation finite-element simulation of displacement-pile installation experiments in sand. *Journal of Geotechnical and Geoenvironmental Engineering*. 2020;146:04020044.
6. Guo N, Zhao J. The signature of shear-induced anisotropy in granular media. *Computers and Geotechnics*. 2013;47:1–15.
7. Zhao J, Guo N. Unique critical state characteristics in granular media considering fabric anisotropy. *Géotechnique*. 2013;63:695–704.
8. Wang R, Dafalias YF, Fu P, Zhang J-M. Fabric evolution and dilatancy within anisotropic critical state theory guided and validated by DEM. *International Journal of Solids and Structures*. 2020;188–189:210–222.
9. Andrade JE, Avila CF, Hall SA, Lenoir N, Viggiani G. Multiscale modeling and characterization of granular matter: from grain kinematics to continuum mechanics. *Journal of the Mechanics and Physics of Solids*. 2011;59:237–250.
10. Guo N, Zhao J. A coupled FEM/DEM approach for hierarchical multiscale modelling of granular media. *International Journal for Numerical Methods in Engineering*. 2014;99:789–818.
11. Nguyen TK, Combe G, Caillerie D, Desrues J. FEM×DEM modelling of cohesive granular materials: numerical homogenisation and multiscale simulations. *Acta Geophysica*. 2014;62:1109–1126.
12. Liu Y, Sun W, Yuan Z, Fish J. A nonlocal multiscale discrete-continuum model for predicting mechanical behavior of granular materials. *International Journal for Numerical Methods in Engineering*. 2016;106:129–160.
13. Desrues J, Argilaga A, Caillerie D, et al. From discrete to continuum modelling of boundary value problems in geomechanics: An integrated FEM-DEM approach. *International Journal for Numerical and Analytical Methods in Geomechanics*. 2019;43:919–955.
14. Guo N, Zhao J. Multiscale insights into classical geomechanics problems. *International Journal for Numerical and Analytical Methods in Geomechanics*. 2016;40:367–390.
15. Guo N, Zhao J, Sun WC. Multiscale analysis of shear failure of thick-walled hollow cylinder in dry sand. *Géotechnique Letters*. 2016;6:77–82.
16. Wu H, Zhao J, Guo N. Multiscale insights into borehole instabilities in high-porosity sandstones. *Journal of Geophysical Research: Solid Earth*. 2018;123:3450–3473.
17. Wu H, Guo N, Zhao J. Multiscale modeling and analysis of compaction bands in high-porosity sandstones. *Acta Geotechnica*. 2018;13:575–599.
18. Wu H, Papazoglou A, Viggiani G, Dano C, Zhao J. Compaction bands in Tuffeau de Maastricht: insights from X-ray tomography and multiscale modeling. *Acta Geotechnica*. 2020;15:39–55.
19. Guo N, Zhao J. Parallel hierarchical multiscale modelling of hydro-mechanical problems for saturated granular soils. *Computer Methods in Applied Mechanics and Engineering*. 2016;305:37–61.
20. Wang K, Sun W. A semi-implicit discrete-continuum coupling method for porous media based on the effective stress principle at finite strain. *Computer Methods in Applied Mechanics and Engineering*. 2016;304:546–583.
21. Wu H, Zhao J, Guo N. Multiscale modeling of compaction bands in saturated high-porosity sandstones. *Engineering Geology*. 2019;261:105282.
22. Zhao S, Zhao J, Lai Y. Multiscale modeling of thermo-mechanical responses of granular materials: A hierarchical continuum–discrete coupling approach. *Computer Methods in Applied Mechanics and Engineering*. 2020;367:113100.
23. Hu Y, Randolph MF. A practical numerical approach for large deformation problems in soil. *International Journal for Numerical and Analytical Methods in Geomechanics*. 1998;22:327–350.
24. Kardani M, Nazem M, Sheng D, Carter JP. Large deformation analysis of geomechanics problems by a combined *rh*-adaptive finite element method. *Computers and Geotechnics*. 2013;49:90–99.
25. Bui HH, Fukagawa R, Sako K, Ohno S. Lagrangian meshfree particles method (SPH) for large deformation and failure flows of geomaterial using elastic-plastic soil constitutive model. *International Journal for Numerical and Analytical Methods in Geomechanics*. 2008;32:1537–1570.
26. Peng C, Wu W, Yu H-S, Wang C. A SPH approach for large deformation analysis with hypoplastic constitutive model. *Acta Geotechnica*. 2015;10:703–717.

27. Sołowski WT, Sloan SW. Evaluation of material point method for use in geotechnics. *International Journal for Numerical and Analytical Methods in Geomechanics*. 2015;39:685–701.

28. Soga K, Alonso E, Yerro A, Kumar K, Bandara S. Trends in large-deformation analysis of landslide mass movements with particular emphasis on the material point method. *Géotechnique*. 2016;66:248–273.

29. Song X, Khalili N. A peridynamics model for strain localization analysis of geomaterials. *International Journal for Numerical and Analytical Methods in Geomechanics*. 2019;43:77–96.

30. Zhu F, Zhao J. A peridynamic investigation on crushing of sand particles. *Géotechnique*. 2019;69:526–540.

31. Liu C, Sun Q, Yang Y. Multi-scale modelling of granular pile collapse by using material point method and discrete element method. *Procedia Engineering*. 2017;175:29–35.

32. Liang W, Zhao J. Multiscale modeling of large deformation in geomechanics. *International Journal for Numerical and Analytical Methods in Geomechanics*. 2019;43:1080–1114.

33. Zhang W, Yuan W, Dai B. Smoothed particle finite-element method for large-deformation problems in geomechanics. *International Journal of Geomechanics*. 2018;18:04018010.

34. Yuan W-H, Wang B, Zhang W, Jiang Q, Feng X-T. Development of an explicit smoothed particle finite element method for geotechnical applications. *Computers and Geotechnics*. 2019;106:42–51.

35. Franci A, Cremonesi M, Perego U, Oñate E. A Lagrangian nodal integration method for free-surface fluid flows. *Computer Methods in Applied Mechanics and Engineering*. 2020;361:112816.

36. Yuan W-H, Liu K, Zhang W, Dai B, Wang Y. Dynamic modeling of large deformation slope failure using smoothed particle finite element method. *Landslides*. 2020;17:1591–1603.

37. Idelsohn SR, Oñate E, Del Pin F. The particle finite element method: a powerful tool to solve incompressible flows with free-surfaces and breaking waves. *International Journal for Numerical Methods in Engineering*. 2004;61:964–989.

38. Oñate E, Idelsohn SR, Del Pin F, Aubry R. The particle finite element method – An overview. *International Journal of Computational Methods*. 2004;1:267–307.

39. Liu GR, Nguyen-Thoi T, Nguyen-Xuan H, Lam KY. A node-based smoothed finite element method (NS-FEM) for upper bound solutions to solid mechanics problems. *Computers & Structures*. 2009;87:14–26.

40. Idelsohn SR, Oñate E, Del Pin F, Calvo N. Fluid–structure interaction using the particle finite element method. *Computer Methods in Applied Mechanics and Engineering*. 2006;195:2100–2123.

41. Dávalos C, Cante J, Hernández J, Oliver J. On the numerical modeling of granular material flows via the particle finite element method (PFEM). *International Journal of Solids and Structures*. 2015;71:99–125.

42. Aubry R, Idelsohn S, Oñate E. Particle finite element method in fluid-mechanics including thermal convection–diffusion. *Computers & Structures*. 2005;83:1459–1475.

43. Cremonesi M, Franci A, Idelsohn S, Oñate E. A state of the art review of the particle finite element method (PFEM). *Archives of Computational Methods in Engineering*. 2020;27:1709–1735.

44. Puso MA, Chen JS, Zywicz E, Elmer W. Meshfree and finite element nodal integration methods. *International Journal for Numerical Methods in Engineering*. 2008;74:416–446.

45. Cortis M, Coombs W, Augarde C, Brown M, Brennan A, Robinson S. Imposition of essential boundary conditions in the material point method. *International Journal for Numerical Methods in Engineering*. 2018;113:130–152.

46. Newmark NM. A method of computation for structural dynamics. *Journal of the Engineering Mechanics Division*. 1959;85:67–94.

47. Hinton E, Rock T, Zienkiewicz OC. A note on mass lumping and related processes in the finite element method. *Earthquake Engineering & Structural Dynamics*. 1976;4:245–249.

48. Edelsbrunner H, Mücke EP. Three-dimensional alpha shapes. *ACM Transactions on Graphics*. 1994;13:43–72.

49. Zhang X, Krabbenhoft K, Sheng D. Particle finite element analysis of the granular column collapse problem. *Granular Matter*. 2014;16:609–619.

50. Zhang X, Krabbenhoft K, Pedroso DM, et al. Particle finite element analysis of large deformation and granular flow problems. *Computers and Geotechnics*. 2013;54:133–142.

51. Kim N-H. *Introduction to Nonlinear Finite Element Analysis*. 1 ed. Springer US; 2014.

52. Šmilauer V, et al. Using and Programming. In: *Yade Documentation*. 2nd ed. The Yade Project; 2015.

53. Guo N, Zhao J. 3D multiscale modeling of strain localization in granular media. *Computers and Geotechnics*. 2016;80:360–372.

54. Potyondy DO, Cundall PA. A bonded-particle model for rock. *International Journal of Rock Mechanics and Mining Sciences*. 2004;41:1329–1364.

55. Kruyt NP, Rothenburg L. Statistical theories for the elastic moduli of two-dimensional assemblies of granular materials. *International Journal of Engineering Science*. 1998;36:1127–1142.

56. Hert S, Seel M. dD Convex Hulls and Delaunay Triangulations. In: *CGAL Editorial Board*. 5.0.2 ed. CGAL Editorial Board; 2020.

57. Oden JT, Pires EB. Algorithms and numerical results for finite element approximations of contact problems with non-classical friction laws. *Computers & Structures*. 1984;19:137–147.

58. Simo JC, Laursen TA. An augmented lagrangian treatment of contact problems involving friction. *Computers & Structures*. 1992;42:97–116.

59. Lu K, Coombs WM, Augarde CE, Hu Z. An implicit boundary finite element method with extension to frictional sliding boundary conditions and elasto-plastic analyses. *Computer Methods in Applied Mechanics and Engineering*. 2020;358:112620.

60. Geuzaine C, Remacle JF. Gmsh: a 3-D finite element mesh generator with built-in pre- and post-processing facilities. *International Journal for Numerical Methods in Engineering*. 2009;79:1309–1331.

61. Gross L, Bourgouin L, Hale AJ, Mühlhaus H-B. Interface modeling in incompressible media using level sets in Escript. *Physics of the Earth and Planetary Interiors*. 2007;163:23–34.

62. Zhao J, Guo N. The interplay between anisotropy and strain localisation in granular soils: a multiscale insight. *Géotechnique*. 2015;65:642–656.

63. Vesić AS. Analysis of ultimate loads of shallow foundations. *Journal of the Soil Mechanics and Foundation Division*. 1973;99:45–73.

64. van der Meij R. *D-Stability User Manual*. 20.1 ed. Netherlands: Deltares; 2019.

65. Zhao S, Zhao J, Liang W. A thread-block-wise computational framework for large-scale hierarchical continuum-discrete modeling of granular media. *International Journal for Numerical Methods in Engineering*. 2020; accepted, https://doi.org/10.1002/nme.6549.